Pore-filling of spiro-OMeTAD in solid-state dye-sensitized solar cells determined via optical reflectometry

Pablo Docampo, Andrew Hey, Stefan Guldin, Robert Gunning, Ullrich Steiner, and Henry J. Snaith

Here, we present an optical probe to determine the pore-filling fraction of the hole-conductor 2,2-7,7-tetrakis-N,N-di-pmethoxyphenylamine-9,9-spirobifluorene (spiro-OMeTAD) into mesoporous photoanodes in solid-state dye-sensitized solar cells (ss-DSCs). Based on refractive index determination by the film's reflectance spectra, and using effective medium approximations, we can extract the volume fractions of the constituent materials and hence quantify pore-filling. This non-destructive method can be used with complete films and does not require detailed model assumptions. pore-filling fractions of up to 80% were estimated for optimized solid-state DSC photoanodes, which is higher than that previously estimated by indirect methods. Additionally, we have determined transport and recombination lifetimes as a function of the pore-filling fraction via photovoltage and photocurrent decay measurements. While extended electron lifetimes were observed with increasing pore-filling fractions, no trend was found in the transport kinetics. The data suggests that a pore-filling fraction of at least 60% is necessary to achieve optimized performance in ss-DSCs. This degree of pore-filling is even achieved in 5 µm thick mesoporous photoanodes. We can therefore conclude from this study that pore-filling is not a limiting factor in the fabrication of thick ss-DSCs.

1 Introduction

The dye-sensitized solar cell (DSC)[1,2] is a very attractive low-cost technology for sustainable power conversion. To date, DSCs exhibit power conversion efficiencies close to

Mr. P. Docampo, Mr. A. Hey, Dr. R. Gunning, Dr. H.J. Snaith
Department of Physics, Clarendon Laboratory, University of Oxford, Parks Road, Oxford OX1 3PU, UK
e-mail:h.snaith1@physics.ox.ac.uk

S. Guldin, Prof. U. Steiner
Department of Physics, University of Cambridge,
J. J. Thomson Avenue, Cambridge CB3 0HE, UK

thin film inorganic photovoltaic devices, but for a fraction of the projected production costs.[3,4] The conventional device architecture, as introduced by Grätzel and O'Regan in 1991,[2] is composed of a mesoporous metal oxide which is deposited onto a transparent conductive oxide (TCO), typically fluorine doped tin oxide (FTO). The mesostructure is then sensitized by chemisorption of a light absorbing dye, filled with a regenerating medium, typically an iodine/triiodide based electrolyte, and finally capped with a regenerating counter electrode, such as platinized FTO. Upon photoexcitation, dye molecules transfer electrons to the conduction band (CB) of the metal oxide which are then transported through the mesostructure to the TCO. Meanwhile, the oxidized dye is regenerated by the surrounding redox medium. The use of volatile liquid electrolytes requires elaborate sealing procedures and threatens the long-term stability of the devices.[5] Furthermore, certain redox couples such as the conventionally used iodide tri-iodide are corrosive.[6] As an alternative, a solid-state DSC based on the organic hole transporting molecule (HTM), (2,2(7,7(-tetrakis-(N,N-di-pmethoxyphenylamine)9,9(-spirobifluorene) Spiro-OMeTAD was introduced in 1998.[7] Since the highest occupied molecular orbital of spiro-OMeTAD is deeper that the redox potential of iodide/tri-iodide couple, there is scope to reduce the required potential difference for driving the dye regeneration process, and in turn, achieve higher power conversion efficiencies.[8,9] This should lead to a feasible increase in device efficiency from a theoretical limit of 15% for iodine based DSCs to over 20% with a solid-state HTM.[9] However, the charge recombination in ss-DSCs is 1 to 2 orders of magnitude faster compared to liquid-electrolyte DSCs, which should reduce the achievable open-circuit voltage by 100 to 200mV.[10]

Currently, the best performing ss-DSCs achieve power conversion efficiencies of up to 7.2%,[11] thus still lagging behind DSCs based on a liquid electrolyte, which are now over 12%.[12] The underperformance of ss-DSC is thought to be associated with three main challenges: (i) limited pore-filling of the mesoporous TiO_2 with the HTM to ensure the optimum composition of the photo-active layer,[13–16] (ii) panchromatic absorption of light, which is currently limited by the maximal film thickness of well-performing ss-DSCs,[17] and (iii) efficient charge generation and transport from the excited dye to maximize the current output from the sunlight.[18–25] While issues with efficient charge generation have been extensively addressed (though not resolved) in earlier work,[18–24] the related challenges of effective pore-filling and sufficient panchromatic absorption remains open. The use of novel panchromatic absorbers may extend the absorption range from currently 425-650 nm to 425-940 nm, with a potential gain of 60% extra in short-circuit current and thus a 25%

increase in power conversion efficiency despite the accompanied loss in voltage due to the reduced bandgap of the absorber.[9] However, in order to utilize panchromatic absorbers efficiently, the film thickness needs to exceed the currently practical limit of 2 µm.

The pore-filling mechanism in solid-state dye-sensitized solar cells has recently been the focus of a number of research groups. Several studies suggest that pore-filling is the limiting factor to achieving thick cells (on the order of 5 µm),[13–16] thus reducing effective light absorption by most common sensitizers. It is therefore of central importance to measure this quantity as accurately as possible in order to fully understand whether pore-filling is an important contributing factor for this thickness limitation.

Several strategies to measure pore-filling in solid-state dye-sensitized solar cells have been proposed. One method employs photoinduced absorption spectroscopy, but this only allows determination of the uniformity of "pore wetting" - the actual filling fraction cannot be quantified.[26] A second method estimates the pore-filling fraction by comparing films coated from the same solutions under identical conditions on both flat and porous substrates. Accounting for the initial solution which soaks into the mesoporous film, the pore-filling fraction can be estimated by measuring the film thickness in cross-sectional SEM, assuming that the difference in film thickness reflects the amount of material imbibed into the pores.[13] In a third method the amount of hole-transporter in the mesoporous film is quantified by redissolving the hole transporter in a chlorobenzene solution in a well-defined amount of solvent. Using calibrated absorption spectra of the solution, the molarity of the hole transporter in the solution can be determined. Using estimates for the porosity, film and capping layer thickness of the infiltrated photoanode, the pore-filling fraction can be estimated.[14]

Neither SEM nor photoinduced absorption measurements allow an accurate measurement of the pore-filling fraction. The recently introduced dissolution technique has proven effective, but requires assumptions of the film porosity, the volume fraction of the chemisorbed dye, and the density of the hole transporter, leading to some ambiguity in the results. Furthermore this method destroys the cell. Here, we propose a simple, non-destructive method to determine the pore-filling of mesoporous photoanodes by an optical method. Based on thin film interference, the spectral reflection of the films allows us to determine their refractive indices with a conventional spectrophotometer. Using the Bruggeman effective medium approximation, we can estimate the volume fractions of all of the film components. Furthermore, we propose a simplified method whereby the pore-filling fractions and the capping layer thickness can be measured through the determination of the mean effective

refractive index for a range of hole transporter concentrations in the casting solution. Employing this optical probe we conclude that pore-filling fractions of over 60% are necessary for the efficient operation of solid-state dye-sensitized solar cells, and pore-filling fractions of up to 80% are estimated in the best filled 3 micron thick devices.

2 Results and Discussion

2.1 Estimating the refractive index

When a beam of light travels across an interface between two materials with different refractive indices, it divides into transmitted and reflected components.[27] A diagram of such a beam is schematically represented in **Figure 1** for light incident on a surface at an angle θ_0. The relative fractions of the split beams are given by the Fresnel coefficients, which in the case of normal incidence ($\theta_0 = 0$) reduce to

$$r_{jk} = \frac{n_j - n_k}{n_j + n_k}\ ; \qquad\qquad t_{jk} = \frac{2n_j}{n_j + n_k}; \tag{1}$$

where r_{jk} and t_{jk} are the Fresnel coefficient for reflected and transmitted light from material j into material k, respectively, and n_j is the refractive index of each of the components. For a beam reflected from a thin film as represented in Figure 1, there is a phase difference (Δ) for the component reflected off the back surface with respect to the component reflected from the front surface. For all subsequent reflections, a further phase shift of Δ per internal reflection within the film must also be added. The total amplitude (A_r) of the electric field of the reflected beam is the sum of all individual reflections

$$\begin{aligned}
A_r^0 &= A_0 r_{01} \\
A_r^1 &= A_0 (t_{01} t_{10} r_{12}) e^{i\Delta} \\
A_r^2 &= A_0 (t_{01} t_{10} r_{12}^2 r_{10}) e^{2i\Delta} \\
A_r^3 &= A_0 (t_{01} t_{10} r_{12}^3 r_{10}^2) e^{3i\Delta} \\
&\vdots \\
A_r^j &= A_0 (t_{01} t_{10} r_{12}^j r_{10}^{j-1}) e^{ji\Delta}
\end{aligned}$$

$$A_r = A_r^0 + A_r^1 + A_r^2 + \cdots = A_0 \left(r_{01} + \left(t_{01} t_{10} \sum_{j=1}^{\infty} r_{12}^j r_{10}^{j-1} e^{ji\Delta} \right) \right) \tag{2}$$

$$r_{01} = -r_{10} \text{ and } t_{01} t_{10} = \sqrt{1 - r_{01}}\sqrt{1 - r_{10}} = 1 - r_{01}^2. \tag{3}$$

Combining eqs. 2 and 3 gives

$$A_r = A_0 \frac{r_{01} + r_{12} e^{i\Delta}}{1 + r_{12} r_{10} e^{i\Delta}}. \tag{4}$$

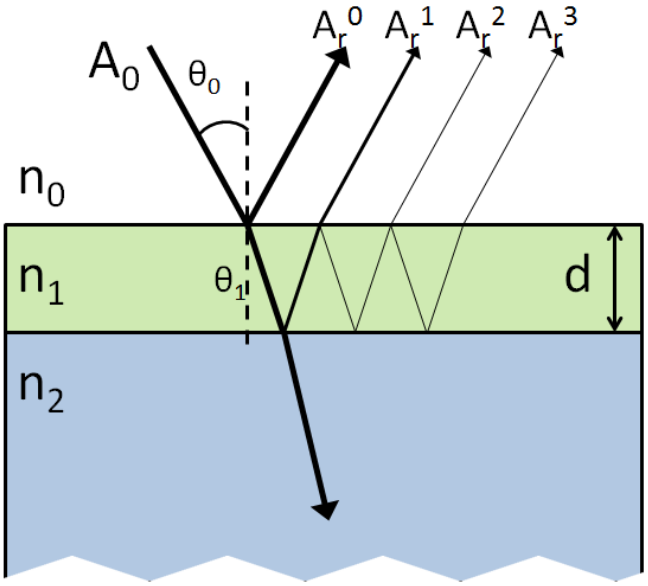

Figure 1. Schematic illustration of the multiple reflections occurring at the interfaces of a thin film.

The reflectance of the film is defined as $R = |A_r/A_0|^2$, hence

$$R = \frac{r_{10}^2 + 2r_{12}r_{01}cos\Delta + r_{12}^2}{1 + 2r_{12}r_{01}cos\Delta + r_{10}^2 r_{12}^2}, \tag{5}$$

with

$$\Delta = \frac{4\pi d n_1}{\lambda} \tag{6}$$

and λ the wavelength of light for a film thickness d. R in eq. (5) has a local maximum for each maximum of $cos\Delta$ and eq. (6) can be used to determine the relative positions of two consecutive wavelength maxima λ_1, λ_2[28]

$$\Delta_1 - \Delta_2 = \frac{4\pi d n_1}{\lambda_1} - \frac{4\pi d n_1}{\lambda_2} = 2\pi. \tag{7}$$

From eq. (7) the refractive index of the film is determined[29]

$$n_1 = \frac{1}{2d\left(\frac{1}{\lambda_1} - \frac{1}{\lambda_2}\right)}. \tag{8}$$

In dispersive media, such as TiO_2, the refractive index also depends on the incident wavelength, but it can be approximated by Cauchy's relation[30]

$$n = A + \frac{B}{\lambda^2} + \frac{C}{\lambda^4} + \cdots. \tag{9}$$

Thus, the wavelength-dependent refractive index of the films can be determined by measuring the reflectance of a film by measuring the positions of consecutive maxima and minima and eq. (8). The refractive index as a function of wavelength is then extracted by fitting the first two terms of the Cauchy function (eq. (9)) to the results of eq. (8). **Figure**

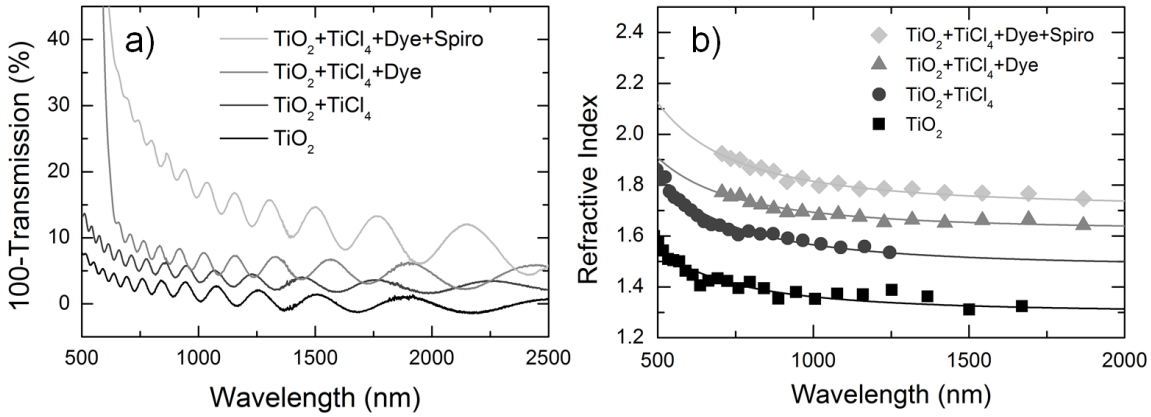

Figure 2. a) Reflectance and b) refractive index versus wavelength of bare mesoporous TiO_2 films (black, squares), after surface treatment with $TiCl_4$ (dark grey, circles), chemisorption of a dye layer (grey, triangles), and infiltration with spiro-OMeTAD (light grey, diamonds). The lines in b) correspond to fits to the data by Cauchy's equation.

2a shows the reflectance spectrum of typical mesoporous TiO_2 films before and after the standard $TiCl_4$ treatment, after dye-sensitization, and filled with spiro-OMeTAD. Figure 2b shows the refractive indices as a function of wavelength (eq. (8)) and a fit using eq. (9). To further validate our data analysis technique, thin films of mesoporous TiO_2 (∼500 nm) were measured by ellipsometry[31] (see Supporting Information). The results of the two techniques show excellent agreement with about a 5% difference at all studied wavelengths. Thicker films could not be measured by ellipsometry due to scattering effects arising from the roughness of the films, as was also found previously.[30]

2.2 Estimating the film composition and pore-filling

The TiO_2 photoanodes used in solid-state dye-sensitized solar cells are composed of nanocrystals about 20 nm in diameter, much smaller than the wavelength of light. The occupied relative volume of TiO_2 and interstitial air voids can therefore be related to the effective refractive index of the film by the Bruggeman's mean field approximation, where v_{air} refers to the volume fraction occupied by air, n_{TiO_2} to the refractive index of anatase TiO_2, and nfilm to the refractive index of the film,[32–34]

$$(1 - v_{\text{air}})\frac{n_{\text{TiO}_2}^2 - n_{\text{film}}^2}{n_{\text{TiO}_2}^2 + 2n_{\text{film}}^2} + v_{\text{air}}\frac{1 - n_{\text{film}}^2}{1 + 2n_{\text{film}}^2} = 0. \tag{10}$$

Using a refractive index of 2.5 for anatase TiO_2 at 600 nm,[33] a porosity $v_{\text{air}} = 62 \pm 1\%$ is extracted for mesoporous films prepared from a TiO_2 nanoparticle paste, which reduces to $v_{\text{air}} = 49 \pm 1\%$ after treatment with an aqueous $TiCl_4$ solution to improve photoanode performance in DSCs.[35,36] Once the porosity of the film is known, a linear approximation can be used to estimate the volume fraction of the remaining components, where v_i and n_i

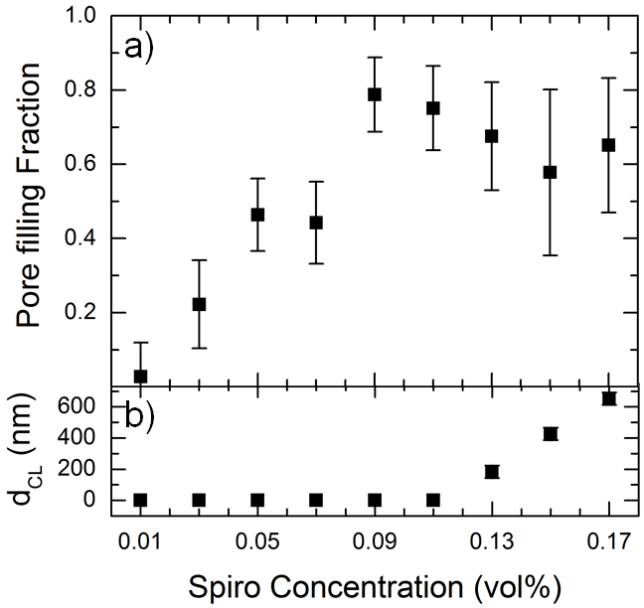

Figure 3. a) pore-filling fraction and b) thickness of capping layer (estimated from SEM images) versus spiro-OMeTAD concentration in the casting solution. The infiltrated materials network consisted of mesoporous TiO_2 with $TiCl_4$ surface treatment, dye and spiro-OMeTAD. Error bars are based on error propagation from the fit to Cauchy's equation.

refer to the volume fraction and refractive index of component i, respectively[37]

$$n_{\mathrm{f}} = \sum_i v_i n_i = v_{\mathrm{air}} n_{\mathrm{air}} + v_{\mathrm{TiO_2}} n_{\mathrm{TiO_2}} + v_{\mathrm{dye}} n_{\mathrm{dye}} + v_{\mathrm{spiro}} n_{\mathrm{spiro}} \tag{11}$$

This linear approximation proves sufficiently accurate for multicomponent systems. To determine the volume fraction of the dye in the system, dye desorption was carried out in a solution of potassium hydroxide in methanol. Measuring the absorption spectrum of the desorbed dye solution (of a controlled solvent volume) allows the determination of the solution molarity and hence amount of chemisorbed dye, and thus its occupied volume in the mesoporous film (assuming that the density of the dye is similar to that of its main indoline constituent component which is approximately 1 g/ml). A refractive index of $n_{\mathrm{dye}} = 1.73 \pm 0.02$ at 600 nm was extracted this way from reflectance measurements of the dye-sensitized films for the indoline based dye D102. The refractive index of a thin film of spiro-OMeTAD was determined from the reflectance spectra (see Supporting Information). The determined value of $n_{\mathrm{spiro}} = 1.93 \pm 0.03$ at 600 nm is in reasonable agreement with other organic semiconductors used in photovoltaic devices.[38]

Once a solution of a sufficiently high concentration of spiro-OMeTAD is spin-coated onto a mesoporous film, a capping layer typically forms on top of the infiltrated layer. The optical system has therefore to be extended to account for this extra layer of spiro-OMeTAD. However, the refractive index of the active layer with maximum pore-filling and the refractive index of spiro-OMeTAD are rather similar (2.11 and 1.93, respectively at 600

	n at 600 nm
n_{TiO_2}[33]	2.5
n_{dye}	1.73 ±0.02
n_{spiro}	1.93 ±0.03
n_{film} (air/TiO_2+$TiCl_4$)	1.73 ±0.02
n_{film} (air/TiO_2+$TiCl_4$/dye)	1.81 ±0.02
n_{film} (air/TiO_2+$TiCl_4$/dye/spiro)	2.11 ±0.03
v_{dye}	0.04 ±0.03
v_{TiO_2}	0.52 ±0.01
v_{spiro}	0.33±0.05
v_{air}	0.10
pore-filling fraction	0.78±0.11

Table 1. Summary of the refractive indices and volume fractions of each of the components in an optimized photoanode.

nm), and interference effects arising from the two-layer stack can as a first approximation be neglected. The difference in phase between two consecutive maxima at normal incidence can therefore be written as

$$\Delta_1 - \Delta_2 = \frac{4\pi(d_{TiO_2} n_f + n_{spiro} d_{CL})}{\lambda_1} - \frac{4\pi(d_{TiO_2} n_f + n_{spiro} d_{CL})}{\lambda_2} = 2\pi. \tag{12}$$

where d_{TiO_2} is the thickness of the mesoporous TiO_2 layer, d_{CL} the thickness of the spiro-OMeTAD capping layer, and n_{CL} its contribution to the refractive index

$$n_f = \frac{1}{2d_{TiO_2}(\frac{1}{\lambda_1} - \frac{1}{\lambda_2})} - \frac{n_{spiro} d_{CL}}{d_{TiO_2}} \tag{13}$$

$$n_{CL} = \frac{n_{spiro} d_{CL}}{d_{TiO_2}}. \tag{14}$$

Figure 3a shows the pore-filling fractions for different concentrations of the spiro-OMeTAD casting solution, using eq. (11). To extract the refractive index of the films when no capping layer is present, eq. (8) was used, and once this layer has formed, eq. (13) was employed. To monitor the capping layer thickness, cross-sectional SEM images of all samples were taken (see Supplementary Information), and the results are summarized in Figure 3b.

Table 1 summarizes the volume fractions and refractive indices of the different components of an optimized photoanode.

The method presented here is a relatively straightforward route to estimate the pore-filling fraction in DSCs. It relies only on the assumption that the pore-filling is uniform from top to bottom, which is well supported by previous literature and cross-sectional SEM.[13,14,39] However, beyond measuring the pore-filling of manufactured films, it would be useful to have a predictive tool which to estimate the pore-filling for given coating

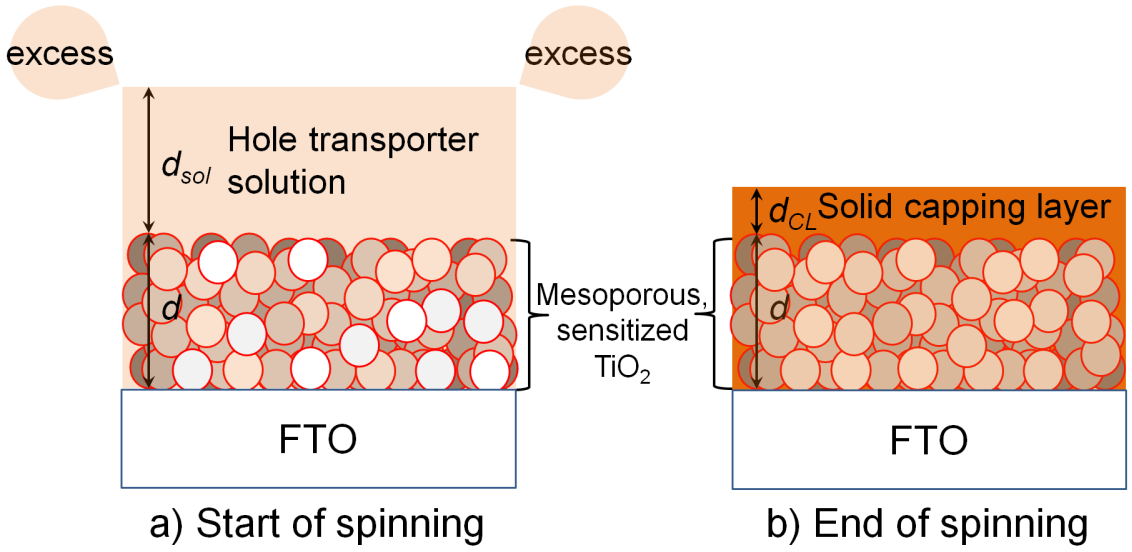

Figure 4. Schematic representation of the spin-coating process. a) In the initial stages of spin-coating, a large quantity of solution flows off the substrate and a solution layer of uniform thickness (d_{sol}) is formed above the mesoporous substrate prior to solvent evaporation. b) After evaporation of all solvent, a solid capping layer of uniform thickness (d_{CL}) remains on top of the infiltrated network.

conditions. Crucial parameters for coating and pore-filling are the film porosity, coating spin-speed, environment temperature and atmosphere, solvent viscosity, hole-transporter concentration in the solvent (c) and solution viscosity as a function of hole-transporter concentration.[40] For a given spin-speed and coating environment, the hole-transporter concentration is the main parameter which can be tuned to optimize the pore-filling. Since the solution viscosity does not change significantly with spiro-OMeTAD concentration, an expression for the filling fraction as a function of solution concentration (c) can be formulated.

When coating a mesoporous film of thickness d and porosity p the total amount of spiro-OMeTAD available to fill the pores is the sum of the amount of dissolved material that is soaked into the mesoporous film ($d \cdot c \cdot p$), plus the amount of material dissolved in the solution film on top of the mesoporous layer before the start of spin-coating ($c \cdot d_{\mathrm{sol}}$), with d_{sol} the initial thickness of this solution layer before solvent evaporation starts. After complete drying and film formation, any of the available material which has not infiltrated into the mesoporous film forms a solid capping layer with thickness d_{CL}. A schematic of this process is shown in **Figure 4**. Hence, as described elsewhere, the pore-filling fraction (PF) can be written as[13]

$$PF = c + \frac{d_{\mathrm{sol}}c - d_{\mathrm{CL}}}{dp}. \tag{15}$$

Using this equation to fit the data in Figure 3a, a solution layer thickness of 6.9 ± 0.5 µm was extracted, which is consistent with other reports in the literature.[13,14] The determina-

tion of the concentration of the spiro-OMeTAD:chlorobenzene solution requires knowledge of the density of spiro, which was determined by re-dissolving films of Spiro-OMeTAD of known thickness and area in chlorobenzene, and then taking UV-visible absorption spectra of the resulting solution to deduce the concentration (see Experimental Section) and hence the mass for a known sample volume. This gave a value of 1.02 ± 0.03 g cm^{-3}, in agreement with previous estimates.[13] Note that this value is significantly different from 1.82 g cm^{-3} obtained by Ding et al. by measuring the mass of a silicon wafer before and after coating with Spiro-OMeTAD.[14] We believe this has introduced an error in their concentration values leading to a significant underestimation of the pore-filling fractions they have reported. So far, the method described requires the determination of the refractive index from consecutive spectral fringes, which is then fitted to a Cauchy function, while the capping layer thickness has to be determined by an alternative method. Unfortunately, this requires additional measurements by SEM or other optical instruments, and introduces an additional source of error since the capping layer estimation is subject to local thickness variations. Furthermore this does not allow the direct determination of pore-filling in a production setting. It should however be possible to monitor the capping layer thickness by its optical footprint in UV-Vis reflectance. As apparent from Figure 3a, the concentration at which the pores are optimally filled corresponds to the concentration at which the capping layer starts to form. As soon as this layer appears, secondary cosine terms arising from the interface between the capping layer and the filled mesoporous layer become visible. This should allow the extraction of the capping layer thickness. Unfortunately, the refractive indices of these two layers are very similar and the available wavelength range is limited. For these reasons the accurate determination of the capping layer by an interference technique is practically impossible. A simpler option is to define an effective refractive index for a film of fixed thickness $d = d_{\mathrm{TiO_2}}$ where the contribution from the capping layer is integrated with that of the filled mesoporous layer using eq. (13). By combining eqs. (8), (11) and (15), assuming that the pore-filling fraction remains approximately constant after the formation of the capping layer and using from eq. (13) that the contribution from the capping layer scales as n_{CL},

$$n_{\mathrm{eff}} = \begin{cases} v_{\mathrm{pores}} + v_{\mathrm{TiO_2}} n_{\mathrm{TiO_2}} + v_{\mathrm{dye}} n_{\mathrm{dye}} + (n_{\mathrm{spiro}} - 1) \frac{1+d_{\mathrm{sol}}}{d_{\mathrm{TiO_2}} v_{\mathrm{pores}}} v_{\mathrm{pores}} c & \text{if } d_{\mathrm{CL}} = 0 \\ n_{eff,CL=0} + \frac{n_{\mathrm{spiro}} d_{\mathrm{CL}}}{d_{\mathrm{TiO_2}}} & \text{if } d_{\mathrm{CL}} \neq 0, \end{cases} \tag{16}$$

where $n_{\mathrm{eff,CL=0}}$ is the maximum refractive index of the film before the capping layer forms. It is clear from this equation that the effective refractive index of the film scales as a

function of the refractive index of spiro-OMeTAD, the solution layer thickness, thickness of TiO_2 and the volume of the pores with increasing spiro-OMeTAD concentration when no capping layer is present. Once this layer forms, the effective refractive index has an additional additive component which scales with n_{CL}. Finding the concentration at which maximum pore-filling occurs is then a simple matter of plotting the effective refractive index versus spiro-OMeTAD concentration and determining the point at which the slope changes. Furthermore, using this simple effective refractive index approximation, accurate values for the capping layer thickness can also be extracted since the gradient of the effective refractive index versus concentration after capping layer formation is proportional to d_{CL}. SEM measurements show that the capping layer thickness increases linearly with solution concentration

$$d_{\mathrm{CL}} = A + Bc, \tag{17}$$

where A is the equivalent solid thickness of the spiro-OMeTAD in the pores at the maximum pore-filling. Experimental results show that the mean effective refractive index ($n_{\mathrm{av,eff}}$) averaged over in the spectral region where none of the constituent components absorb (650 to 2500 nm in the present system) is a reliable measure to quantify pore-filling

$$n_{\mathrm{av,eff}} = \frac{N}{2d_{\mathrm{TiO_2}}\left(\frac{1}{\lambda_1} - \frac{1}{\lambda_2}\right)} \tag{18}$$

where N is the number of observed maxima. Based on dye desorption experiments, a mean refractive index of $n_{\mathrm{dye}} = 1.65$ was extracted for the D102 dye. For spiro-OMeTAD an average value of $n_{\mathrm{spiro}} = 1.81$ was determined from reflectometry measurements of a flat film (see Supporting Information). Finally, a mean refractive index of 2.17 over the spectral range was determined from the experimental data for the mesoporous TiO_2 layer. **Figure 5a** shows the mean effective refractive index for a range of concentrations. A clear change in slope is found for concentrations above which a capping layer is formed (grey circles). The light grey line shows the prediction of the mean effective refractive index using eq. (16), with $d_{\mathrm{sol}} = 6.9$ µm, extracted from the data in Figure 3a, and the parameters for the capping layer thickness A=-1340 and B=11740 nm (eq. 17) extracted from SEM measurements (see Supporting Information).

The two presented methods to extract the pore-filling fraction of the films, (1) using wavelength dependent refractive index, shown in Figure 3a, and (2) using the mean effective

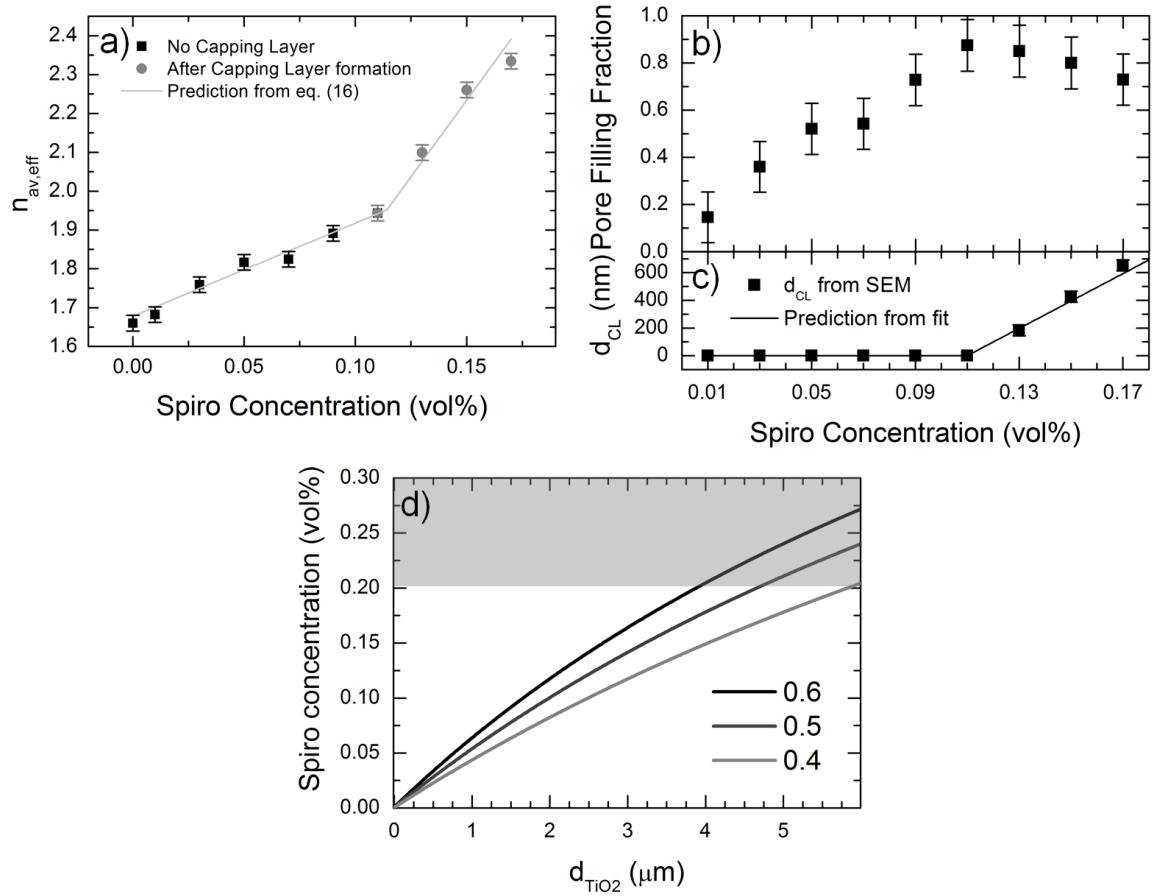

Figure 5. (a) Refractive index of the infiltrated films as a function of the spiro-OMeTAD concentration in the casting solution. Data points prior to the formation of a capping layer are shown as black squares, once a capping layer has formed data points are shown as grey circles. The light grey line corresponds to the theoretical prediction using d_{sol} from Figure 3a and eq. (16). (b) Determined pore-filling fractions as a function of the spiro-OMeTAD concentration based on the mean effective refractive index and eq. (11). Error bars are estimated from the typical standard deviation found for 4 different substrates. (c) Capping layer thickness as a function of casting spiro-OMeTAD concentration from SEM image analysis. The black line corresponds to the capping layer extracted from (a). d) Estimation of the spiro-OMeTAD casting concentration that result in optimally filled pores as a function of the thickness of the mesostructured electrode and for a range of pore volume fractions. To calculate these concentrations, d_{sol} was taken as 7.2 µm, and a maximum pore-filling fraction of 80% was assumed. The grey area corresponds to the solubility limit of spiro-OMeTAD in chlorobenzene. In this regime, the solution is not perfectly clear.

refractive index, can be evaluated for consistency. Indeed, the slope of $n_{\mathrm{av,eff}}$ prior to the formation of a capping layer (black squares in Figure 5a) corresponds to a solution layer thickness $d_{\mathrm{sol}} = 7.2 \pm 0.3$ µm, which lies within experimental error of $d_{\mathrm{sol}} = 6.9 \pm 0.5$ µm found from the data of Figure 3a. Figure 5b shows the pore-filling fraction as a function of spiro-OMeTAD concentration determined from the mean, effective refractive index of Fig. 5a. This method results in a much smaller error in pore-filling faction compared to the data presented in Figure 3a. A linear fit to the data for concentrations above which the capping layer has formed (grey circles in Figure 5a) allows the extraction of the capping layer thickness, shown in Figure 5c, which is in excellent agreement with the thicknesses determined from SEM cross-sectional images . Figure 5d shows the predicted concentration of spiro-OMeTAD which results in optimally filled pores as a function of film thickness and for a range of relative pore volumes. This calculation is based on the assumption that d_{sol} is not dependent on spiro-OMeTAD concentration, relative pore volume and thickness of the mesoporous TiO_2 layer, and on a spin-coating speed of 700 rpm. It is very interesting to note that a reduced porosity is predicted to improve pore-filling in thick films. This counter-intuitive prediction will be explored in a future study. The concentration for which the highest pore-filling is achieved is clearly discernible from Fig. 5a, i.e.no further analysis is needed for experimental pore-filling optimization. Note that if the solution viscosity varies considerably with spiro-OMeTAD concentration, the relationship between d_{sol} and concentration needs to be determined and added to the pore-filling relation, eq. (15). The observation of a linear scaling of pore-filling with concentration however indicates that there is no significant change in d_{sol} with the concentration in the studied range.

2.3 Solid-state dye-sensitized solar cells

In order to relate the effects of pore-filling to the photovoltaic performance, solid-state dye-sensitized solar cells were fabricated from a variety of spiro-OMeTAD concentrations in the casting solution resulting in different pore-filling fractions. The resulting J-V curves are shown in **Figure 6**, where a steady increase in short circuit current with increasing pore-filling is found, up to a maximum of 6.0 mA cm^{-2} at the spiro-OMeTAD concentration corresponding to the highest pore-filling fraction. A further increase in spiro-OMeTAD concentration in the casting solution has only a minimal effect on the short circuit current, but lower fill-factor of the cells is observed, indicating an increase in series-resistance, which is probably due to the increasing thickness of the spiro-OMeTAD capping layer. The maximum in power conversion efficiency of 3.2% was obtained for cells made with a 9%

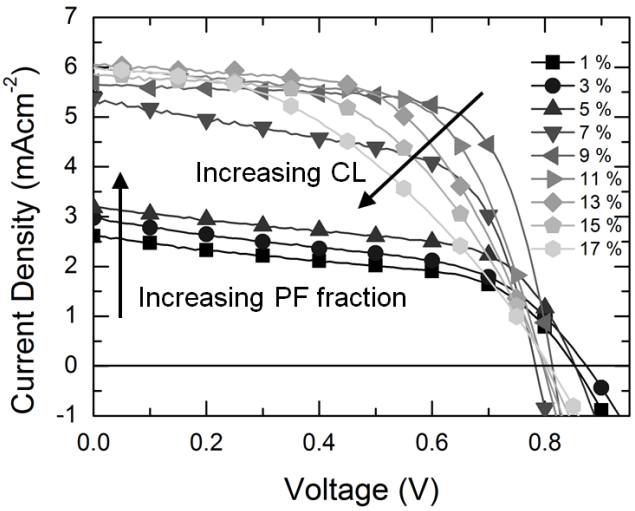

Figure 6. Current density versus voltage for solid-state dye-sensitized solar cells fabricated with different vol% concentrations of spiro-OMeTAD measured under AM1.5 simulated sun light of 100mWcm^{-2} irradiance. Lighter shades of grey indicate higher concentrations. CL refers to the capping layer thickness.

c (vol%)	PF_{meas}	PF_{fit}	J_{SC}	η	V_{OC}	FF	d_{CL} (SEM)	d_{CL} (fit)
1	0.006	0.007	0.2	0.1	0.73	0.36	-	-
3	0.16	0.20	3.0	1.3	0.87	0.5	-	-
5	0.25	0.35	3.2	1.6	0.85	0.58	-	-
7	0.57	0.48	5.4	2.5	0.78	0.59	-	-
9	0.72	0.62	5.7	3.2	0.81	0.71	-	-
11	0.85	0.78	6.0	3.1	0.80	0.66	-	-
13	0.83	0.78	6.0	2.7	0.80	0.57	180	197
15	0.80	0.78	5.9	2.4	0.80	0.52	420	395
17	0.80	0.78	6.0	2.0	0.81	0.42	650	592

Table 2. Photovoltaic performance parameters for a range of spiro-OMeTAD casting solution concentrations and their corresponding capping layer thicknesses (d_{CL}) in nm and pore-filling fractions (PF). PF_{meas} refers to the values extracted from the reflectometry measurements and PF_{fit} to the expected values from the fitted d_{sol}.

spiro-OMeTAD solution, which is close to the concentration for the optimum pore-filling of 11% with a power conversion efficiency of 3.1%, lying well within experimental error in solution concentration and power conversion efficiency. The results are summarized in Table 2.

To further probe the charge carrier kinetics of the devices, photovoltage and photocurrent decay measurements at short circuit conditions were performed for cells made from a variety of spiro-OMeTAD concentrations, shown in **Figure 7**. We can clearly see a trend of prolonged recombination lifetimes with increasing pore-filling fractions up to the highest pore-filling fraction (above 9 vol% spiro-OMeTAD, which is equivalently to a pore-filling fraction of ∼60%). All cells made from higher spiro-concentrations have similar electron lifetimes, with overlapping points at all studied bias light intensities. These results are in good agreement with a study by Melas-Kyriazi et al, where improved pore-filling was

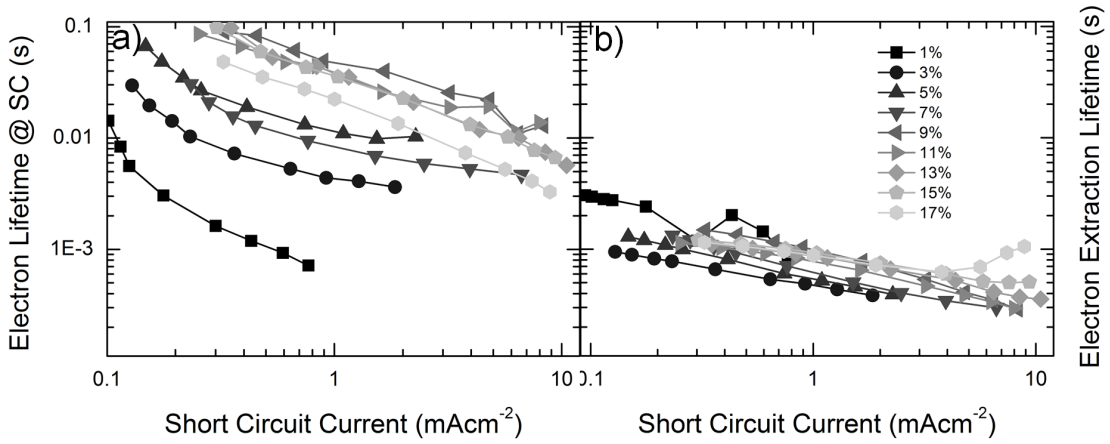

Figure 7. Photovoltage (a) and photocurrent (b) decay measurements at short circuit conditions versus short circuit current for a range of spiro-OMeTAD solution concentrations.

found to extend the electron lifetime at short circuit to around 10 ms.[41] While the electron lifetime increases for high pore-filling fractions, no trend was observed in the extraction lifetimes at high light bias, as shown in Figure 6b, where most measurement points overlap. Long lifetimes are only observed once the capping layer has formed, which allows establishing a correlation between capping layer thickness and electron extraction time at high light bias. Following results from the device and pore-filling study, a pore-filling fraction with Spiro-OMeTAD of at least 60% is required to achieve optimized performance in solid-state dye-sensitized solar cells. In order to probe the upper limit for photoanode infiltration, 5.05 µm thick TiO_2 films were subjected to the $TiCl_4$ treatment and filled using solutions with a range of spiro-OMeTAD concentrations. A pore-filling fraction of 62 ± 11% was measured (see Supporting Information) for the highest concentration used in this study, proving that sufficient pore-filling of thick mesoporous films is in fact possible, and the performance limitation of devices with thick photoanodes is due to poor charge collection related to the high recombination rates exhibited by this type of solar cell.[25,42,43] Further studies optimising the composition of the hole-transporter and further changes in device architecture to inhibit recombination in thick films may alleviate this issue.

3 Conclusions

In summary, we have developed an optical technique based on thin film interference to reliably measure the pore-filling fraction of mesoporous photoanodes used in solid-state dye-sensitized solar cells. By determining the refractive index from the reflectance spectrum of the films and fitting the resulting values with a Cauchy function, the volume fraction of the constituent materials was extracted. This non-destructive method can be used for mesoporous films at the various stages of the fabrication process and does not require

any assumptions of material properties. pore-filling fractions of up to 80% were found for optimized photoanodes. A second even more straight-forward analysis is based on the definition of an "overall effective refractive index", which allows the direct determination of the maximum pore-filling fraction for a range of hole-transporter solution concentrations. The photovoltage and photocurrent decay techniques were used to determine the charge carrier transport and recombination lifetimes at short-circuit conditions as a function of pore-filling. With increasing pore-filling fractions, the lifetime of electrons was extended, while no trend was found in the transport kinetics. The main result of this work is that a pore-filling fraction of at least 60% is required to achieve optimized performance in solid-state dye-sensitized solar cells. Since it is possible to optimally fill mesoporous films of up to 5 µm in thickness, the performance limitation of thick devices must stem from other factors, such as the poor electron transport in these nanocrystalline TiO_2 networks combined with the high recombination rates which are characteristic for devices using spiro-OMeTAD as the hole transporter. Further work is still required however to fully understand the thickness limitations "beyond pore-filling".

4 Experimental

Spiro density determination

To obtain the density of Spiro-OMeTAD, films were spin-cast from chlorobenzene onto glass slides. Film thicknesses were measured using a Dektak 150 surface profiler, and the glass was cut after coating with spiro-OMeTAD in order to remove any edges where increased film thickness is often observed and potential coating of the sides and the underside of the slides. The areas of the films were then measured using high resolution photography, allowing the volume of each film to be determined accurately. The Spiro-OMeTAD was then re-dissolved in a known volume of chlorobenzene and UV-visible absorption spectra were taken for the resulting solutions. The spectrum was also taken for a solution containing a known mass of Spiro-OMeTAD in chlorobenzene (see Supporting Information). From this, the molar extinction coefficient ϵ for a given wavelength was obtained via the Beer-Lambert law $A = c\epsilon l$,[44] where A is absorbance, c solution concentration and l the optical path length. By comparing the spectra from the dissolved films at the same wavelength, the concentration and hence the mass of the dissolved Spiro-OMeTAD in the film was attained, and since the film volume is also known, the density was determined.

Substrate preparation for pore-filling measurements

2mm thick glass was cut down to the required size for screen printing. A commercial

anatase nanoparticle paste (Dyesol 18NR-T) was diluted with anhydrous terpineol at a ratio of 0.3g of terpineol per 1g of paste to obtain final film thicknesses of around 1.8 µm per layer when deposited by screen-printing. The resulting films were subsequently calcined at 500 °C (ramped over 1.5 hours) for 30 minutes in air. The substrates were then immersed in a 15 mM $TiCl_4$ solution at 70 °C for 1 hour, and were subsequently baked once more at 500 °C for 45 min in air, then cooled down to 70 °C and finally immersed in a dye solution for 1 hour. The dye solution used was formed by an indoline-based dye, termed D102, dissolved in a mixture of 1:1 by volume of acetonitrile and *tert*-butanol.

Optical characterization

Ellipsometric determination of optical constants was carried out on a spectroscopic ellipsometer (Woollam alpha-SE, spectral range 380 nm-900 nm) and fitting of the data using the manufacturer's software. Reflectance spectra were collected with a Perkin-Elmer Lambda 9 UV-Vis-NIR Spectrophotometer with a dual beam setup.

Solid-state dye-sensitized solar cells preparation

Fluorine doped tin oxide (FTO) coated glass sheets (15 Ω/□ Pilkington) were etched with zinc powder and HCl (2 M) to obtain the required electrode pattern. The sheets were then washed with soap (2% Hellmanex in water), de-ionized water, acetone, and methanol and finally treated under oxygen plasma for 10 minutes to remove the last traces of organic residues. The FTO sheets were subsequently coated with a compact layer of TiO_2 (100 nm) by aerosol spray pyrolysis deposition at 450 °C, using air as the carrier gas. Deposition of mesoporous TiO_2 and dyeing on the device substrates was conducted as described above. 2,2',7,7'-tetrakis(N,N-di-p-methoxypheny-amine)-9,9'-spirobifluorene (Spiro-OMeTAD) was dissolved in chlorobenzene at a range of concentrations. After fully dissolving the hole transporter, 4-*tert*-butyl pyridine (*t*BP) was added (76 mM). Lithium bis(trifluoromethylsulfonyl)imide salt (Li-TFSI) was pre-dissolved in acetonitrile at 170 mg ml^{-1} and added to the hole transporter solution (25 mM). Importantly, the *t*BP and Li-TFSI molarity was held constant in the solution, and not held constant with respect to the spiro-OMeTAD concentration. The dyed films were rinsed briefly in acetonitrile and dried in air for 1 minute. For spin-coating, a small quantity of the hole transporter solution (90 µl) was dispensed and homogeneously spread by means of a pipette onto a block of 4 substrates, taking care to not exceed 15 seconds for the spreading procedure, and was immediately spin-coated at 700 rpm for 40 s in air, at which point the solvent has completely evaporated from most of the block. A second step at 2000 rpm for 2 seconds was used to remove the excess solvent which tends to accumulate in the corners before slowing

down. The films were left overnight in an air atmosphere before placing them in a thermal evaporator where 150 nm thick silver electrodes were deposited through a shadow mask under high vacuum (10^{-6} mbar). The active areas of the devices were defined by metal optical masks with 0.09 to 0.125 cm^2 apertures.

Solar cell characterization

Solar simulated AM 1.5 sunlight was generated with an ABET class AAB solar simulator calibrated to give 100 mW cm^{-2} using an NREL calibrated KG5 filtered silicon reference cell. The spectral mismatch factor was calculated to be less than 1%. The JV curves were recorded with a Keithley 2400. The Solar Cells were masked with a metal aperture defining the active area of the solar cells. The photovoltage decay measurement was performed by a similar method to O'Regan et al[45] and as described elsewhere.[13,19,46]

5 Acknowledgements

This project was part funded by EPSRC First Grant Scheme EP/F065884/1 and European Community's Seventh Framework Programme (FP7/2007-2013) under grant agreement n° 246124 of the SANS project.

References

[1] M. Grätzel, *Journal of Photochemistry and Photobiology a-Chemistry* **2004**, *164*(1-3), 3–14.

[2] B. Oregan, M. Grätzel, *Nature* **1991**, *353*(6346), 737–740.

[3] Y. Chiba, A. Islam, Y. Watanabe, R. Komiya, N. Koide, L. Y. Han, *Japanese Journal of Applied Physics Part 2-Letters & Express Letters* **2006**, *45*(24-28), L638–L640.

[4] A. Kay, M. Grätzel, *Solar Energy Materials and Solar Cells* **1996**, *44*(1), 99–117.

[5] G. Boschloo, A. Hagfeldt, *Accounts of Chemical Research* **2009**, *42*(11), 1819–1826.

[6] E. Olsen, G. Hagen, S. Eric Lindquist, *Solar Energy Materials and Solar Cells* **2000**, *63*(3), 267–273.

[7] U. Bach, D. Lupo, P. Comte, J. E. Moser, F. Weissortel, J. Salbeck, H. Spreitzer, M. Grätzel, *Nature* **1998**, *395*(6702), 583–585.

[8] J. N. Clifford, E. Palomares, M. K. Nazeeruddin, M. Grätzel, J. R. Durrant, *The Journal of Physical Chemistry C* **2007**, *111*(17), 6561–6567.

[9] H. J. Snaith, *Advanced Functional Materials* **2010**, *20*(1), 13–19.

[10] H. J. Snaith, L. Schmidt-Mende, M. Grätzel, M. Chiesa, *Physical Review B* **2006**, *74*(4), 045306.

[11] J. Burschka, A. Dualeh, F. Kessler, E. Baranoff, N.-L. Cevey-Ha, C. Yi, M. K. Nazeeruddin, M. Grätzel, *Journal of the American Chemical Society* **2011**, *133*(45), 18042–18045.

[12] A. Yella, H. W. Lee, H. N. Tsao, C. Y. Yi, A. K. Chandiran, M. K. Nazeeruddin, E. W. G. Diau, C. Y. Yeh, S. M. Zakeeruddin, M. Grätzel, *Science* **2011**, *334*(6056), 629–634.

[13] H. J. Snaith, R. Humphry-Baker, P. Chen, I. Cesar, S. M. Zakeeruddin, M. Grätzel, *Nanotechnology* **2008**, *19*(42), 424003.

[14] I. K. Ding, N. Tetreault, J. Brillet, B. E. Hardin, E. H. Smith, S. J. Rosenthal, F. Sauvage, M. Grätzel, M. D. McGehee, *Adv. Func. Matter.* **2009**, *19*(15), 2431–2436.

[15] H. Snaith, L. Schmidt-Mende, *Adv. Mater.* **2007**, *19*(20), 3187–3200.

[16] L. Schmidt-Mende, M. Grätzel, *Thin Solid Films* **2006**, *500*(12), 296–301.

[17] L. Schmidt-Mende, S. M. Zakeeruddin, M. Grätzel, *Applied Physics Letters* **2005**, *86*(1), 013504.

[18] P. Docampo, M. Stefik, S. Guldin, R. Gunning, N. A. Yufa, N. Cai, P. Wang, U. Steiner, U. Wiesner, H. J. Snaith, *Advanced Energy Materials* **2012**, , n/a–n/a.

[19] P. Docampo, S. Guldin, M. Stefik, P. Tiwana, M. C. Orilall, S. Huttner, H. Sai, U. Wiesner, U. Steiner, H. J. Snaith, *Adv. Funct. Mater.* **2010**, *20*(11), 1787 – 1796.

[20] Y. Tachibana, J. E. Moser, M. Grätzel, D. R. Klug, J. R. Durrant, *Journal of Physical Chemistry* **1996**, *100*(51), 20056–20062.

[21] J. Kroeze, N. Hirata, L. Schmidt-Mende, C. Orizu, S. Ogier, K. Carr, M. Grätzel, J. Durrant, *Advanced Functional Materials* **2006**, *16*(14), 1832–1838.

[22] J. E. Kroeze, N. Hirata, S. Koops, M. K. Nazeeruddin, L. Schmidt-Mende, M. Grätzel, J. R. Durrant, *Journal of the American Chemical Society* **2006**, *128*(50), 16376–16383.

[23] S. Koops, B. O'Regan, P. R. F. Barnes, J. R. Durrant, *J. Am. Chem. Soc* **2009**, *131*(13), 4808–4818.

[24] A. Abrusci, R. S. Santosh Kumar, M. Al-Hashimi, M. Heeney, A. Petrozza, H. J. Snaith, *Advanced Functional Materials* **2011**, *21*(13), 2571–2579.

[25] S. Guldin, S. Huttner, P. Tiwana, M. C. Orilall, B. Ulgut, M. Stefik, P. Docampo, M. Kolle, G. Divitini, C. Ducati, S. A. T. Redfern, H. J. Snaith, U. Wiesner, D. Eder, U. Steiner, *Energy & Environmental Science* **2011**, *4*(1), 225–233.

[26] U. B. Cappel, E. A. Gibson, A. Hagfeldt, G. Boschloo, *Journal of Physical Chemistry C* **2009**, *113*(15), 6275–6281.

[27] M. Born, *Cambridge University Press 7th Edition*, –.

[28] P. D. T. Huibers, D. O. Shah, *Langmuir* **1997**, *13*(22), 5995–5998.

[29] C. Pickering, M. I. J. Beale, D. J. Robbins, P. J. Pearson, R. Greef, *Thin Solid Films* **1985**, *125*(12), 157–163.

[30] A. J. Moule, H. J. Snaith, M. Kaiser, H. Klesper, D. M. Huang, M. Grätzel, K. Meerholz, *Journal of Applied Physics* **2009**, *106*(7), 073111–9.

[31] S. Guldin, M. Kolle, M. Stefik, R. Langford, D. Eder, U. Wiesner, U. Steiner, *Advanced Materials* **2011**, *23*(32), 3664–3668.

[32] D. A. G. Bruggeman, *Ann. Phys.* **1935**, *24*(7), 636–664.

[33] S. Y. Kim, *Applied Optics* **1996**, *35*(34), 6703–6707.

[34] M. Khardani, M. Bouaicha, B. Bessas, *physica status solidi (c)* **2007**, *4*(6), 1986–1990.

[35] P. M. Sommeling, B. C. O'Regan, R. R. Haswell, H. J. P. Smit, N. J. Bakker, J. J. T. Smits, J. M. Kroon, J. A. M. van Roosmalen, *The Journal of Physical Chemistry B* **2006**, *110*(39), 19191–19197.

[36] B. C. O'Regan, J. R. Durrant, P. M. Sommeling, N. J. Bakker, *The Journal of Physical Chemistry C* **2007**, *111*(37), 14001–14010.

[37] J. R. Birchak, C. G. Gardner, J. E. Hipp, J. M. Victor, *Proceedings of the IEEE* **1974**, *62*(1), 93–98.

[38] N.-K. Persson, M. Sun, P. Kjellberg, T. Pullerits, O. Inganas, *The Journal of Chemical Physics* **2005**, *123*(20), 204718–9.

[39] A. Abrusci, I. K. Ding, M. Al-Hashimi, T. Segal-Peretz, M. D. McGehee, M. Heeney, G. L. Frey, H. J. Snaith, *Energy & Environmental Science* **2011**, *4*(8), 3051–3058.

[40] R. K. Yonkoski, D. S. Soane, *Journal of Applied Physics* **1992**, *72*(2), 725–740.

[41] J. Melas-Kyriazi, I. K. Ding, A. Marchioro, A. Punzi, B. E. Hardin, G. F. Burkhard, N. Tétreault, M. Grätzel, J.-E. Moser, M. D. McGehee, *Advanced Energy Materials* **2011**, *1*(3), 407–414.

[42] F. Fabregat-Santiago, J. Bisquert, L. Cevey, P. Chen, M. Wang, S. M. Zakeeruddin, M. Grätzel, *J. Am. Chem. Soc.* **2009**, *131*(2), 558–562.

[43] S. Guldin, P. Docampo, M. Stefik, G. Kamita, U. Wiesner, H. J. Snaith, U. Steiner, *Small* **2012**, *8*(3), 432–440.

[44] J. D. Ingle, S. R. Crouch, *Prentice Hall 1st edition* , .

[45] B. C. O'Regan, F. Lenzmann, *J. Phys. Chem. B.* **2004**, *108*(14), 4342–4350.

[46] J. Bisquert, A. Zaban, M. Greenshtein, I. Mora-Seró, *Journal of the American Chemical Society* **2004**, *126*(41), 13550–13559.

6 Supporting Information

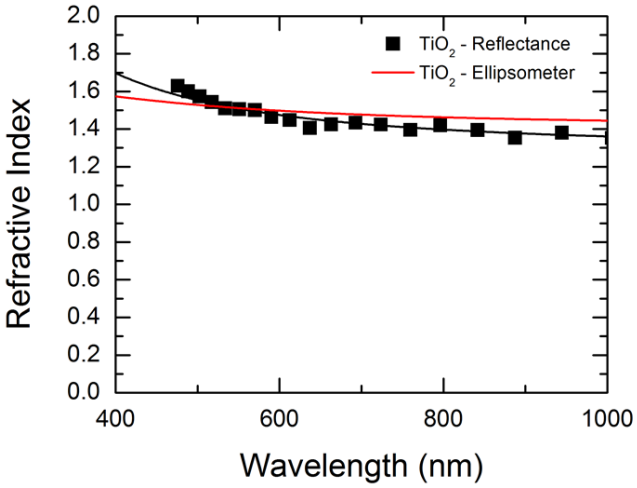

Figure 8. Refractive index as a function of wavelength determined from the reflectance spectrum (black squares) and measured with a spectroscopic ellipsometer (red line). The black line is the fit of a Cauchy function to the points determined from the reflectance spectrum.

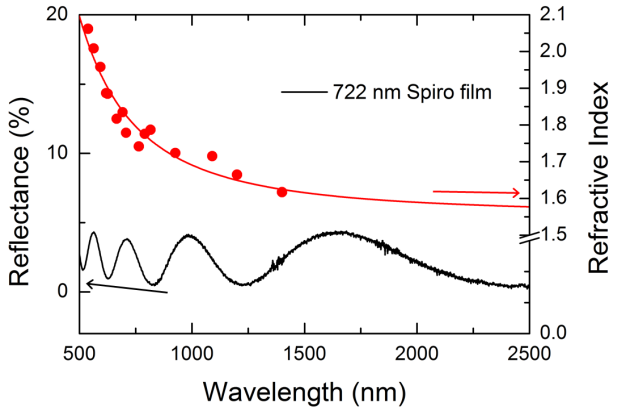

Figure 9. Reflectance (left) and refractive index (right) versus wavelength of a thick 722 nm spiro-OMeTAD film. The red line corresponds to the fit of a Cauchy function.

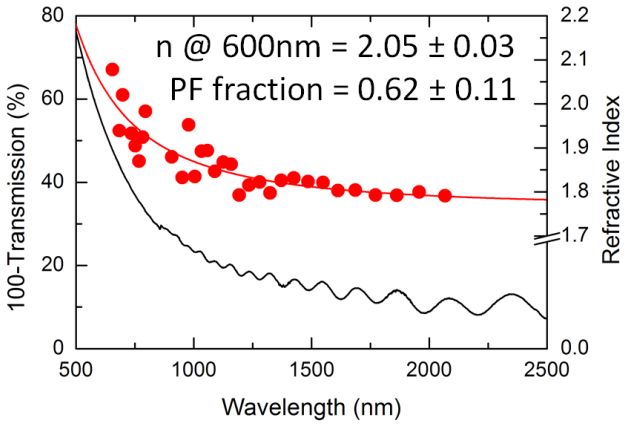

Figure 10. Transmittance (left) and refractive index (right) versus wavelength for a 5.05 µm thick film filled with spiro-OMeTAD from a 17 vol% solution (without dye). The red line corresponds to the fit of a Cauchy function.

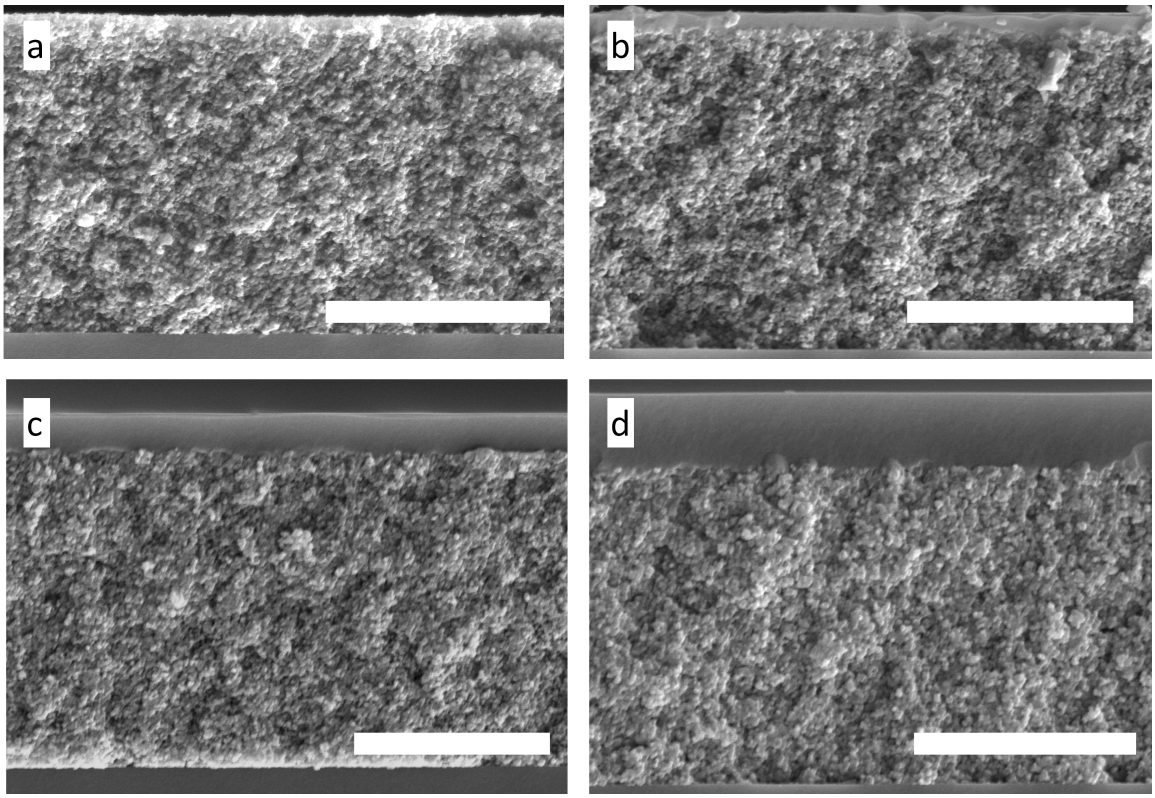

Figure 11. Cross-sectional SEM images of mesoporous TiO_2, after $TiCl_4$ treatment, with dye and filled from solutions of a) 11%, b) 13%, c) 15% and d) 17% of spiro-OMeTAD. Scale bars correspond to a length of 2 µm.

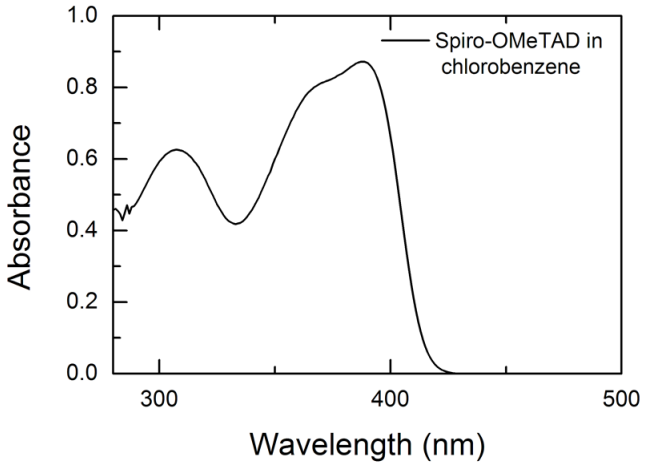

Figure 12. UV-visible absorption spectrum of 0.014 mM Spiro-OMeTAD dissolved in chlorobenzene.